Journal of Advanced Materials Research
http://dx.doi.org/10.62762/JAMR.2026.189146

RESEARCH ARTICLE

Crystal-Field Analysis and Temperature-Dependent Luminescence Mechanism of Broadband Near-Infrared $Na_3Al_2Li_3F_{12}:Cr^{3+}$ Phosphors

Xinlei Zang[1,2], Yagang Feng[1,*], Yumeng Li[1], Ziyu Liu[3], Lei Duan[1], Shichang Cai[1], Hanlu Zhang[1], Chen Hu[2,4], Zhenzhen Zhou[2,4], Denis Yu. Kosyanov[5] and Jiang Li[2,4,*]

[1] School of Materials Science and Engineering, Henan University of Technology, Zhengzhou 450007, China
[2] State Key Laboratory of High Performance Ceramics, Shanghai Institute of Ceramics, Chinese Academy of Sciences, Shanghai 201899, China
[3] School of Materials Science and Engineering, Changsha University of Science & Technology, Changsha 410114, China
[4] Center of Materials Science and Optoelectronics Engineering, University of Chinese Academy of Sciences, Beijing 100049, China
[5] Far Eastern Federal University, Vladivostok 690922, Russia

Abstract

Garnet-structured fluoride phosphors are attractive for phosphor-converted near-infrared light-emitting diodes (NIR pc-LEDs) owing to their broadband emission and thermal stability. Herein, pure-phase $Na_3Al_{2-x}Cr_xLi_3F_{12}$ (x = 0–0.16; NALF:Cr^{3+}) phosphors were synthesized hydrothermally, and their structure, morphology, crystal field, and luminescence were systematically investigated. Crystal-field analysis yielded a Dq/B of ~2.18, confirming a weak crystal-field environment for Cr^{3+}. Under 430 nm excitation, all samples show a broad NIR band over 650–900 nm with a FWHM of ~101 nm, ascribed to the $^4T_{2g} \rightarrow {}^4A_{2g}$ transition. Fluorescence decay and time-resolved emission spectroscopy indicate that Cr^{3+} solely replaces octahedral Al^{3+}, forming a single luminescent center, optimal at x = 0.08. The phosphor retains over 67% of its room-temperature intensity at 423 K, and temperature-dependent photoluminescence reveals the zero-phonon line (ZPL) of the $^4T_{2g} \rightarrow {}^4A_{2g}$ transition at 80 K, offering deeper insight into the Cr^{3+} luminescence mechanism in fluoride garnets. NALF:Cr^{3+} is thus a promising broadband NIR phosphor for blue-LED-pumped pc-LEDs.

Keywords: Cr^{3+}, fluoride phosphor, $Na_3Al_2Li_3F_{12}$, near-infrared emission, luminescence dynamics, temperature-dependent photoluminescence.

Submitted: 11 July 2026
Revised: 29 August 2026
Accepted: 03 September 2026
Published: 20 September 2026

Vol. 2, **No.** 3, 2026.
10.62762/JAMR.2026.189146

***Corresponding authors:**
✉ Yagang Feng
yagangfeng@haut.edu.cn
✉ Jiang Li
lijiang@mail.sic.ac.cn

Citation
Zang, X., Feng, Y., Li, Y., Liu, Z., Duan, L., Cai, S., Zhang, H., Hu, C., Zhou, Z., Kosyanov, D. Y., & Li, J. (2026). Crystal-Field Analysis and Temperature-Dependent Luminescence Mechanism of Broadband Near-Infrared $Na_3Al_2Li_3F_{12}:Cr^{3+}$ Phosphors. *Journal of Advanced Materials Research*, 2(3), 285–298.

1 Introduction

Near-infrared (NIR) light, characterized by low photon energy, strong penetration through biological tissues, and minimal environmental interference, has attracted increasing attention due to its unique optical properties [1, 2]. It has been widely applied in areas such as plant lighting, non-destructive testing, and night vision technologies [3, 4]. Conventional NIR light sources, including halogen lamps, gas-discharge lamps and traditional laser diodes, have difficulty meeting modern application demands. NIR pc-LEDs have emerged as a promising alternative due to their compact structure, energy efficiency, environmental friendliness, highly tailorable emission spectra, and long operational lifetime, becoming one of the most active research directions in the field of NIR light sources [5, 6]. To date, a variety of transition-metal and rare-earth ions, such as Cr^{3+}, Mn^{4+}, Eu^{2+}, Fe^{3+}, Yb^{3+}, Er^{3+}, and Nd^{3+}, have been extensively investigated for realizing NIR emission [7–13].

Cr^{3+} ions, with a $3d^3$ electronic configuration, are highly sensitive to the crystal-field environment and exhibit good spectral overlap with commercial LED chip emission, making them one of the most widely used activator ions for NIR phosphors [14–17]. In a weak crystal-field environment, the $^4T_2$ level becomes the lowest excited state. After excitation from the ground state ($^4A_2$) to higher-lying excited states such as ^2E or $^4T_1$, the electrons undergo rapid non-radiative relaxation to the $^4T_2$ state, followed by a spin-allowed $^4T_2 \rightarrow {}^4A_2$ radiative transition, resulting in broadband NIR emission typically spanning 650–1200 nm [18, 19]; intervalence charge transfer between Cr^{3+}–Cr^{3+} pairs at elevated concentrations can furthermore extend the emission into the NIR-II region [20]. This broad emission coverage closely matches the requirements of NIR pc-LED applications, making Cr^{3+} an ideal activator for NIR phosphor materials.

Cr^{3+}-doped garnet-structured phosphors represent a class of highly efficient NIR-emitting materials. The open crystal structure of garnet hosts provides sufficient structural flexibility for homogeneous Cr^{3+} incorporation and effective crystal-field tuning [21]. As a result, Cr^{3+}-activated garnet-based NIR phosphors have been extensively investigated in various systems, including $Gd_3Al_2Ga_3O_{12}:Cr^{3+}$, $Y_3In_2Ga_3O_{12}:Cr^{3+}$, and $Gd_3Sc_2Ga_3O_{12}:Cr^{3+}$ [22–24]. Current research on Cr^{3+}-activated materials primarily focuses on broadband emission tuning and enhancement of thermal stability. Compared with oxide hosts [25], fluoride materials generally possess lower phonon energies (typically below 400 cm^{-1}, significantly lower than the 800–1000 cm^{-1} range of oxides). The reduced phonon energy effectively weakens electron–phonon coupling, thereby suppressing non-radiative relaxation processes and improving both photoluminescence efficiency and thermal stability [26–29]. In addition, in fluoride hosts, the $^4T_2$ level of Cr^{3+} is typically lower than the ^2E level, which facilitates efficient $^4T_2 \rightarrow {}^4A_2$ broadband emission and further enhances NIR luminescence performance [30, 31].

$Na_3Al_2Li_3F_{12}$ (NALF) is a typical garnet-structured fluoride host featuring low phonon energy, high crystallinity, and a stable framework. In Cr^{3+}-doped NALF phosphors, Cr^{3+} ions predominantly substitute for Al^{3+} sites, leading to broadband NIR emission in the range of 650–900 nm. The close match in ionic radius and charge between Cr^{3+} (0.615 Å) and Al^{3+} (0.535 Å) results in minimal lattice distortion and a relatively homogeneous dopant distribution [32]. Moreover, this system exhibits not only high quantum efficiency but also excellent resistance to thermal quenching, making NALF: Cr^{3+} a promising research focus in NIR phosphor development.

In 2021, Huang et al. [32] synthesized NALF:Cr^{3+} phosphors with different doping concentrations via a co-precipitation method and analyzed the luminescence dynamics mechanism of Cr^{3+} in detail. Broadband emission from 650 to 1000 nm with a FWHM of approximately 110 nm was achieved. The fabricated device delivered a radiant flux of 14.3 mW under a driving current of 60 mA. In the same year, Nie et al. [33] investigated $Na_3X_2Li_3F_{12}:Cr^{3+}$ (X = Al, Ga, In) systems and demonstrated that In substitution significantly enhances luminescence performance. In particular, $Na_3In_2Li_3F_{12}:Cr^{3+}$ exhibited an emission intensity 5.5 times higher than that of $Na_3Al_2Li_3F_{12}:Cr^{3+}$, with an expanded FWHM of 121 nm. However, the thermal stability of the luminescence of $Na_3In_2Li_3F_{12}:Cr^{3+}$ is significantly poorer than that of $Na_3Al_2Li_3F_{12}:Cr^{3+}$. Existing studies on $Na_3Al_2Li_3F_{12}:Cr^{3+}$ have mainly concentrated on its room-temperature and high-temperature luminescence properties, while the low-temperature photophysical processes and their underlying mechanisms remain poorly understood. In particular, the correlation between the local crystal-field environment, the Cr^{3+} energy-level structure, and the evolution of broadband near-infrared emission with temperature has not been systematically established.

In this work, the phase purity, crystal structure, morphology, and luminescence properties of NALF:Cr^{3+} phosphors were systematically investigated. The local crystal-field environment of Cr^{3+} ions was analyzed based on the absorption spectra and the Tanabe–Sugano diagram, confirming that Cr^{3+} ions reside in a weak crystal-field environment responsible for broadband near-infrared emission. The concentration-dependent luminescence behavior, fluorescence dynamics, time-resolved emission spectra and thermal stability were further studied in detail. These findings offer a more comprehensive understanding of the luminescence mechanism of Cr^{3+}-activated fluoride garnets and provide guidance for the rational design of broadband NIR phosphors.

2 Experimental

A series of $Na_3Al_{2-x}Cr_xLi_3F_{12}$ (x = 0, 0.04, 0.08, 0.12, and 0.16) phosphors were synthesized via a hydrothermal method, following the aqueous synthesis route established for fluoride garnets $Na_3[M_2^{3+}](Li_3)F_{12}$ [34]. The starting materials were weighed according to the stoichiometric composition of $Na_3Al_{2-x}Cr_xLi_3F_{12}$. Firstly, 2 mmol $Al(NO_3)_3{\cdot}9H_2O$ (99%, Macklin, China) and a corresponding amount of $Cr(NO_3)_3{\cdot}9H_2O$ (99%, Macklin, China) were dissolved in deionized water, followed by the addition of 5 mL hydrofluoric acid (HF, mass fraction: 40%, Macklin, China). The mixture was transferred into a polytetrafluoroethylene beaker and magnetically stirred for 20 min to ensure complete dissolution and homogeneity. Subsequently, stoichiometric amounts of NaF (99%, Macklin, China) and LiF (99%, Macklin, China) were added into the solution, and the mixture was continuously stirred for 2 h to promote complete reaction. Next, the precursor solution was transferred into a Teflon-lined stainless-steel autoclave and heated at 200 °C for 12 h. After naturally cooling to room temperature (RT), a green gel-like precipitate was obtained. The product was collected by centrifugation and washed three times with deionized water and ethanol, respectively, to remove residual soluble impurities and improve particle dispersion. Finally, the obtained powder was dried at 80 °C for 10 h in air to yield the final NALF:Cr^{3+} phosphor samples.

The phase structure of the synthesized samples was characterized by X-ray diffraction (XRD) using a diffractometer (D8 Advance, Bruker, Germany) with Cu Kα_1 radiation (λ = 1.5406 Å). The diffraction patterns were collected in the 2θ range of 5–90° with a scanning rate of 5°/min. The morphologies of the samples were investigated using a field emission scanning electron microscope (FESEM, TM4000Plus III, Hitachi, Japan). The optical absorption spectra were measured using a UV-Vis-NIR spectrophotometer (UV2600i, Shimadzu, Japan). The photoluminescence excitation and emission (PLE/PL) spectra of the NALF:Cr^{3+} were recorded using a self-assembled spectroscopic system consisting of a 150 W VX-XBO xenon lamp, an Omni-λ3007 monochromator (Zolix, China), and a PMTH-S1-CR131 photomultiplier tube. An LHM254 mercury lamp was also employed as an auxiliary excitation source when necessary. The time-resolved emission spectra, luminescence decay curves and temperature-dependent PL spectra of the sample with x = 0.08 were tested by a fluorescence spectrophotometer (FLS1000, Edinburgh Instruments, UK) equipped with a 450 W xenon lamp and a temperature-controlled instrument (INSTEC HP1200G, USA).

3 Results and Discussion

The ionic radius matching rule is adopted to evaluate the feasibility of ion substitution in crystalline materials. When the relative radius difference between the dopant (Cr^{3+}) and the substituted host ion is less than 30%, the substitution process is thermodynamically favored, yielding a high probability of forming a stable solid solution with uniform doping. The relative difference in ionic radii is calculated using the following equation (1):

$$D_r = \left| 100\% \times \frac{R_m(N) - R_d(N)}{R_m(N)} \right| \quad (1)$$

In this equation, D_r represents the relative ionic radius difference between the host cation and the dopant ion; R_m and R_d denote the ionic radii of the host cation and the dopant ion, respectively; and N corresponds to the coordination number. According to the ionic radius data of Shannon [35], the ionic radii of Cr^{3+} in tetrahedral, octahedral, and dodecahedral sites are 0.55, 0.615, and 0.755 Å, respectively. The calculated D_r values are 14.95% for the Cr^{3+} (0.615 Å)/Al^{3+} (0.535 Å) pair, 36.02% for the Cr^{3+}/Na^+ (1.180 Å) pair, and 6.78% for the Cr^{3+}/Li^+ (0.590 Å) pair. Taking into account the valence states and ionic radii of all involved cations, Cr^{3+} ions preferentially substitute for Al^{3+} lattice sites in the NALF host.

Since all NALF:Cr^{3+} phosphors exhibit similar appearances, the x = 0.08 sample was selected as a

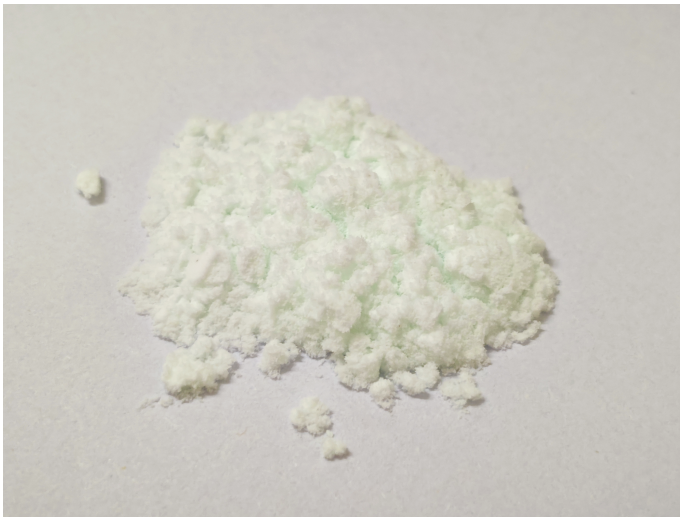

Figure 1. Photograph of the NALF:Cr^{3+} phosphor with $x = 0.08$.

representative to display the physical photograph of the powder. Figure 1 presents the photograph of the NALF:Cr^{3+} phosphor with $x = 0.08$. Under natural daylight, the sample exhibits a pale cyan appearance.

Figure 2(a) illustrates the schematic crystal structure of NALF. In this cubic unit cell, Na^+ ions occupy the dodecahedral sites, Li^+ ions reside in the tetrahedral sites, and Al^{3+} ions are coordinated by six F^- ions, forming $[AlF_6]$ octahedra. Figure 2(b) shows the XRD patterns of the as-prepared NALF:Cr^{3+} phosphors together with the standard pattern of cubic NALF (JCPDS Card No. 71-1219). All diffraction peaks of the doped samples match well with the standard reference, indicating that Cr^{3+} ions are successfully incorporated into the host lattice without inducing any detectable phase transition even at the highest doping concentration ($x = 0.16$). No impurity peaks are observed, confirming the high phase purity of the synthesized phosphors. Furthermore, the Rietveld refinement results for the $x = 0$ and $x = 0.08$ samples, as shown in Figure 2(c) and Figure 2(d), further confirm the high structural quality of the material. The experimental and calculated patterns exhibit good agreement, with a negligible difference curve. The refinement yields reliable agreement factors, with $R_{wp} < 10\%$, $\chi^2 = 2.31$ for $x = 0$ and $\chi^2 = 1.51$ for $x = 0.08$, demonstrating the validity of the structural model. The small residual deviations observed around several intense diffraction peaks are mainly associated with slight discrepancies in peak position and profile shape, which may originate from instrumental broadening, crystallite-size/microstrain effects, and the limitations of the peak profile function.

Table 1. Refined structural data of NALF and NALF:Cr^{3+} phosphors with different Cr^{3+} doping concentrations.

x	Space group	a (Å)	V (Å^3)	R_{wp}	R_p	χ^2
0	$Ia\bar{3}d$	12.1324(2)	1785.85	9.09%	6.48%	2.31
0.04	$Ia\bar{3}d$	12.1255(3)	1782.78	9.96%	7.31%	2.61
0.08	$Ia\bar{3}d$	12.1452(2)	1791.47	8.04%	5.73%	1.51
0.12	$Ia\bar{3}d$	12.1311(2)	1785.26	8.96%	6.26%	2.04
0.16	$Ia\bar{3}d$	12.1294(2)	1784.50	8.04%	5.73%	1.51

Table 1 presents the specific Rietveld refinement results for the NALF and NALF:Cr^{3+} phosphors with different Cr^{3+} doping concentrations. As shown in the table, all the samples are in the cubic garnet structure with the $Ia\bar{3}d$ space group. The refined lattice parameters vary within a narrow range of 12.1255–12.1452 Å. Such a weak and non-monotonic variation may arise from the combined effects of Cr^{3+} substitution at the Al^{3+} octahedral sites, local agglomeration and defect compensation. The subsequent spectroscopic analysis will discuss in detail the potential defects, as well as the possible existence of multiple luminescent centers resulting from substitution at different lattice sites in NALF:Cr^{3+} samples with varying Cr^{3+} doping concentrations.

Figure 3 presents the FESEM micrographs of NALF:Cr^{3+} phosphors with different Cr^{3+} doping concentrations. As observed from the images, particles at all doping levels exhibit a predominantly uniform polyhedral morphology with well-defined grain boundaries, although a small number of fine particles are attached to the surfaces of larger grains. In addition, with increasing Cr^{3+} doping content from $x = 0$ to 0.12, the grain size of the phosphors decreases significantly, with the dominant grain size reducing from approximately 5 μm to about 1 μm. However, when the Cr^{3+} concentration was further increased to $x = 0.16$, no obvious change in particle size was observed, indicating a saturation tendency in the size-refinement effect. This phenomenon, in which the particle size gradually decreases as the Cr^{3+} doping concentration increases, is also observed in other Cr^{3+}-doped fluoride powders [36]. This can be attributed to the increased nucleation rate and inhibited crystal growth caused by Cr^{3+} incorporation. The larger ionic radius of Cr^{3+} compared with Al^{3+} induces local lattice distortion and defect formation, which promotes heterogeneous nucleation while suppressing crystal growth during the hydrothermal process. Consequently, more nuclei are generated and the available growth units are distributed among numerous crystallites, resulting in smaller particle

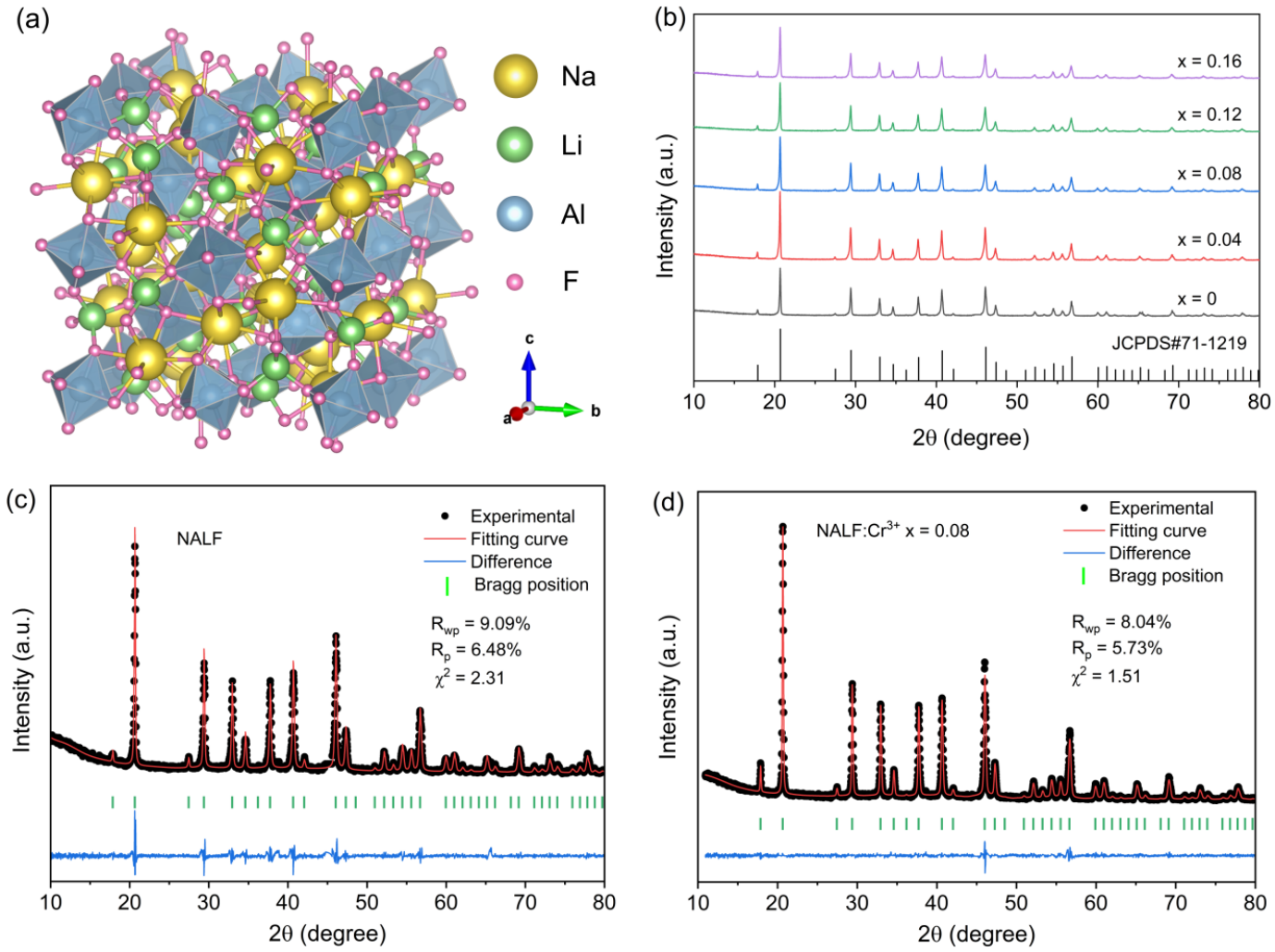

Figure 2. (a) Schematic diagram of the NALF unit cell, (b) XRD patterns of NALF:Cr^{3+} phosphors, and Rietveld refinement results of (c) NALF powder and (d) NALF:Cr^{3+} phosphor with $x = 0.08$.

sizes.

Figure 4 presents the UV-Vis-NIR absorption spectra of NALF:Cr^{3+} phosphors with different Cr^{3+} doping concentrations in the wavelength range of 200–800 nm at RT. As shown, two prominent broad absorption bands can be observed, centered at approximately 430 nm ($^4A_{2g} \rightarrow {}^4T_{1g}$) and 620 nm ($^4A_{2g} \rightarrow {}^4T_{2g}$), respectively, which are attributed to the spin-allowed d–d transitions of Cr^{3+} ions. Both absorption bands exhibit relatively large FWHM values, with the strongest absorption peak located in the blue spectral region, indicating efficient excitation by commercial blue LED chips and suggesting good applicability for blue-pumped broadband NIR phosphors. In addition, the absorption observed in the 200–300 nm range can be attributed to the superposition of the band-gap absorption of the NALF matrix and the characteristic $^4A_{2g} \rightarrow {}^4T_{1g}$ (^4P) absorption of Cr^{3+} ions, and this characteristic transition will be presented in the PLE spectra of NALF:Cr^{3+} shown in Figure 6(a).

From the perspective of the Cr^{3+} luminescence mechanism, its emission behavior is highly dependent on the local crystal-field environment. When Cr^{3+} ions are located in a strong crystal field, the emission is dominated by the spin-forbidden $^2E \rightarrow {}^4A_{2g}$ transition, resulting in sharp-line emission features. In contrast, under a weak crystal field, the energy level of the ^2E state increases relative to the $^4T_{2g}$ state, and radiative relaxation via the spin-allowed $^4T_{2g} \rightarrow {}^4A_{2g}$ transition becomes dominant. In this case, the sharp-line emission is suppressed, and only a broadband NIR emission can be observed. This characteristic is a key prerequisite for achieving broadband near-infrared (NIR) emission from Cr^{3+}-activated phosphors. The crystal-field strength experienced by Cr^{3+} ions can be quantitatively evaluated using the Tanabe–Sugano diagram (Figure 5). Specifically, when the ratio of the

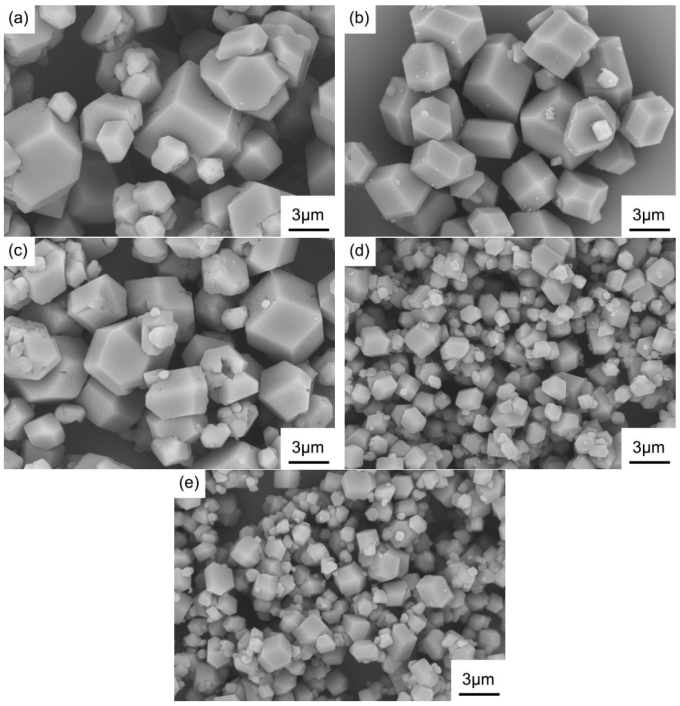

Figure 3. FESEM micrographs of NALF:Cr^{3+} phosphors with different Cr^{3+} doping concentrations: (a) $x = 0$, (b) $x = 0.04$, (c) $x = 0.08$, (d) $x = 0.12$, (e) $x = 0.16$.

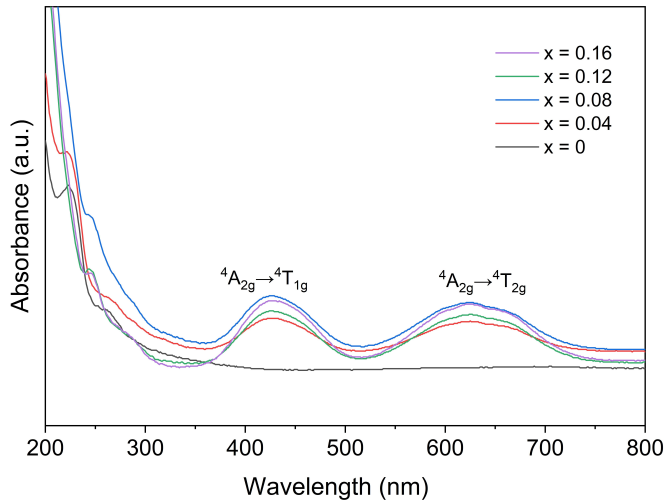

Figure 4. Absorption spectra of NALF:Cr^{3+} phosphors with $x = 0$, 0.04, 0.08, 0.12, and 0.16.

crystal-field splitting parameter (Dq, describing the splitting of the d orbitals under the ligand field) to the Racah parameter (B, representing electron–electron repulsion within the d orbitals) is $Dq/B < 2.3$, the system is classified as a weak crystal field; conversely, when $Dq/B > 2.3$, it corresponds to a strong crystal-field regime. The crystal-field strength at each crystallographic site can be roughly estimated based on the splitting parameter Dq/B, using Eqs. (2)–(4):

$$D_q = \frac{E(^4T_{2g})}{10} = \frac{E(^4A_{2g} \rightarrow {}^4T_{2g})}{10} \tag{2}$$

$$\begin{aligned} \Delta E &= E(^4T_{1g}) - E(^4T_{2g}) \\ &= E(^4A_{2g} \rightarrow {}^4T_{1g}) - E(^4A_{2g} \rightarrow {}^4T_{2g}) \end{aligned} \tag{3}$$

$$\frac{D_q}{B} = \frac{15\,(\Delta E/D_q - 8)}{(\Delta E/D_q)^2 - 10\,\Delta E/D_q} \tag{4}$$

where Dq represents the crystal-field splitting strength and B is the Racah parameter. The energies of the $^4T_{1g}$ and $^4T_{2g}$ levels, $E(^4T_{1g})$ and $E(^4T_{2g})$, were derived from the corresponding absorption peak positions of the $^4A_{2g} \rightarrow {}^4T_{1g}$ (F) and $^4A_{2g} \rightarrow {}^4T_{2g}$ (F) transitions, respectively. For the samples doped with different Cr^{3+} concentrations, the absorption peak positions are similar. Therefore, 430 nm and 620 nm were selected to calculate Dq/B, with corresponding $E(^4T_{1g})$ and $E(^4T_{2g})$ values of 2.88 eV and 2.00 eV, respectively. Based on these values, the Dq/B ratio for all NALF:Cr^{3+} phosphors was calculated to be 2.18, which is slightly lower than the critical value (~2.3) that separates weak and strong crystal-field regimes in classical crystal-field theory. This result clearly indicates that Cr^{3+} ions in the NALF host experience a weak crystal-field environment. According to the Tanabe–Sugano diagram, in the weak crystal-field region, the $^4T_{2g}$ state lies below the ^2E_g state, leading to broadband NIR emission rather than sharp-line emission originating from the $^2E \rightarrow {}^4A_2g$ transition. This emission behavior is fully consistent with the broadband luminescence observed in Figure 6, thereby confirming the $^4T_{2g} \rightarrow {}^4A_{2g}$ transition-dominated mechanism.

Figure 6 presents the PLE/PL spectra of NALF:Cr^{3+} phosphors measured at RT. In the NALF host matrix, Cr^{3+} ions act as luminescent centers and exhibit typical NIR emission arising from spin-allowed d–d transitions. The PLE spectra display three broad excitation bands centered at approximately 280 nm, 430 nm, and 620 nm, which are consistent with the absorption features and correspond to the $^4A_{2g} \rightarrow {}^4T_{1g}$ (^4P), $^4A_{2g} \rightarrow {}^4T_{1g}$ (^4F) and $^4A_{2g} \rightarrow {}^4T_{2g}$ (F) transitions of Cr^{3+} ions, respectively. These excitation bands are in good agreement with the absorption spectra of the NALF:Cr^{3+} phosphors presented in Figure 4. Notably, the excitation band assigned to the $^4A_{2g} \rightarrow {}^4T_{2g}$ transition exhibits a weak fine structure with several superimposed sub-bands. This

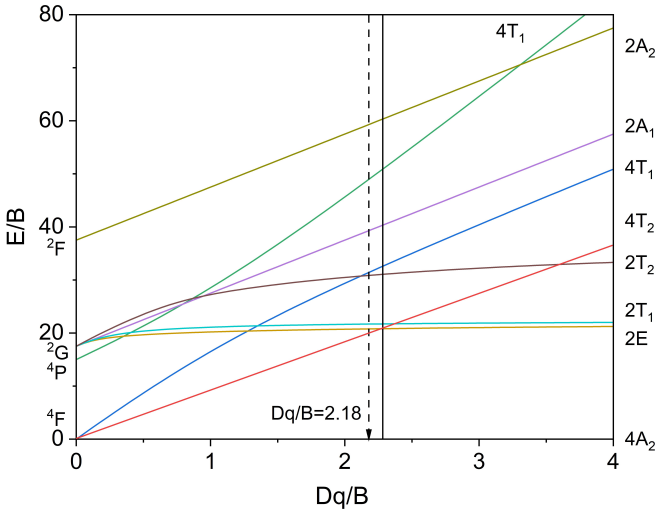

Figure 5. Tanabe–Sugano energy-level diagram for Cr^{3+} in an octahedral crystal field.

behavior can be attributed to the interaction between spin-allowed and spin-forbidden states, as well as the crystal-field splitting of the $^4T_{2g}$ level under a distorted local environment, which leads to a partially resolved vibronic or multiplet structure [37].

Upon 430 nm blue-light excitation, the NALF:Cr^{3+} phosphors exhibit a broad NIR emission band centered at approximately 740 nm, covering the 650–900 nm spectral range, with a FWHM of around 101 nm for all the samples. The FWHM value is consistent with the results reported in the literature [31]. This emission is ascribed to the spin-allowed $^4T_{2g} \rightarrow {}^4A_{2g}$ transition of Cr^{3+} ions. In addition, the emission intensity strongly depends on the Cr^{3+} concentration. The sample with x = 0.08 delivers the strongest emission intensity, while further increasing the Cr^{3+} concentration leads to a gradual decrease in luminescence intensity due to the concentration-quenching effect. To further evaluate the influence of Cr^{3+} concentration on the emission profile, the emission spectra were normalized, as shown in Figure 6(b). The results indicate that all samples exhibit nearly identical spectral shapes, characterized by a single broadband NIR emission centered at ~740 nm, suggesting that Cr^{3+} ions occupy similar crystallographic sites across different doping levels without significant alteration of the local crystal-field environment. Based on the emission intensity results, the optimal Cr^{3+} doping concentration is determined to be x = 0.08. Literature reports indicate that for the garnet-structured $Li_3Na_3Ga_2F_{12}$:Cr^{3+} phosphor, the optimal Cr^{3+} doping concentration is 0.1, which is close to our research findings [27].

The luminescence dynamics of Cr^{3+} ions were

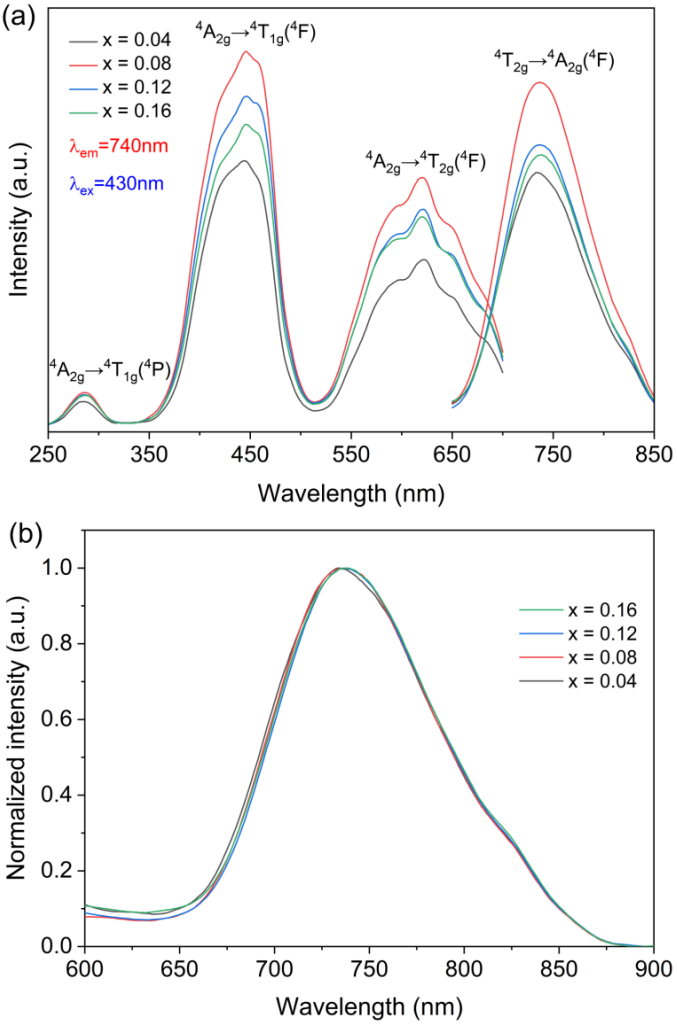

Figure 6. (a) PL and PLE spectra and (b) normalized PL spectra of NALF:Cr^{3+} phosphors measured at RT.

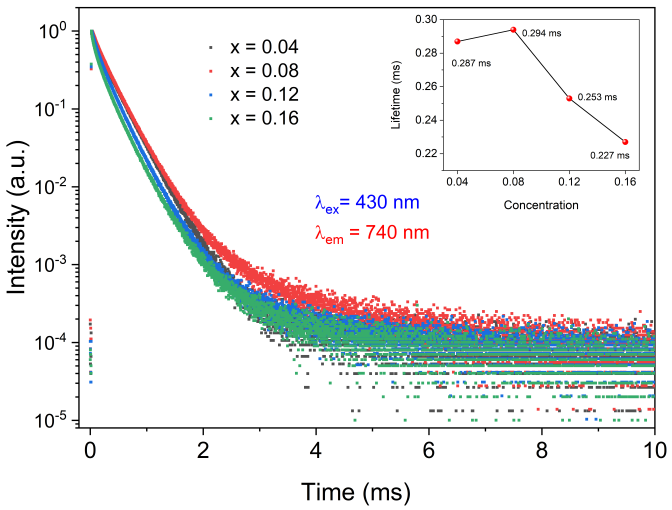

Figure 7. Fluorescence decay curves of NALF:Cr^{3+} phosphors with x = 0.04, 0.08, 0.12, and 0.16.

investigated, and the fluorescence decay curves of NALF: Cr^{3+} phosphors with different Cr^{3+} doping concentrations were measured at RT, as shown in

Figure 7. All decay profiles were recorded under 430 nm excitation by monitoring the characteristic emission peak at 750 nm of Cr^{3+}. The experimental decay curves were well fitted using a biexponential decay model, Eq. (5), to accurately evaluate the fluorescence lifetimes, Eq. (6), of Cr^{3+} ions in the NALF host lattice.

$$I(t) = I_{bg} + A_1 \exp\left(-\frac{t - t_0}{\tau_1}\right) + A_2 \exp\left(-\frac{t - t_0}{\tau_2}\right) \quad (5)$$

$$\tau_{ave} = \frac{A_1\tau_1^2 + A_2\tau_2^2}{A_1\tau_1 + A_2\tau_2} \quad (6)$$

In Eq. (5), $I(t)$ represents the luminescence intensity at time t, I_{bg} is the background intensity offset, and t_0 represents the temporal shift caused by the instrumental response. A_1 and A_2 are the amplitudes of the fast and slow decay components, respectively, while τ_1 and τ_2 correspond to their decay lifetimes. The average lifetime τ_{ave} was calculated accordingly. The results obtained through biexponential fitting were excellent, with corresponding coefficient-of-determination (R^2) values > 0.9999. The detailed fitting parameters are presented in Table 2. It can be concluded that there are two different Cr^{3+} emission environments: one with a relatively fast decay time of approximately 0.10 ms and another with a slower decay time of about 0.30 ms. As the Cr^{3+} concentration increases, the proportion of the fast decay component gradually increases, while the proportion of the slow decay component gradually decreases. The corresponding τ_{ave} values show that the lifetime of Cr^{3+} increases from 0.287 ms at $x = 0.04$ to 0.294 ms at $x = 0.08$, and then gradually decreases to 0.227 ms at $x = 0.16$. By combining the trend of luminescence intensity variation, the reduction in lifetime confirms the occurrence of concentration quenching in heavily doped samples. The increased Cr^{3+} concentration enhances non-radiative relaxation pathways, thereby increasing the probability of energy migration and cross-relaxation processes. As a result, the radiative recombination efficiency is reduced, leading to an accelerated decay process. The concentration-dependent luminescence behavior and the associated lifetime reduction observed here are consistent with previous findings in Cr^{3+}-doped garnet systems, where increasing dopant concentration enhances energy migration and cross-relaxation among neighboring activator ions [38].

Table 2. Relevant parameters obtained from fitting with a biexponential decay function.

Cr^{3+} doping concentration	A_1	τ_1 (ms)	A_2	τ_2 (ms)	R^2
0.04	0.2626	0.0940(4)	0.7888	0.3065(2)	0.99996
0.08	0.3289	0.1183(6)	0.7530	0.3222(4)	0.99995
0.12	0.4752	0.0983(5)	0.6600	0.2903(6)	0.99985
0.16	0.5642	0.0572(3)	0.6313	0.2602(4)	0.99977

The fluorescence decay curves of NALF:Cr^{3+} phosphors can be satisfactorily fitted using a biexponential function, suggesting the coexistence of two relaxation components. To further clarify the origin of the biexponential decay, time-resolved emission spectroscopy (TRES) of the NALF:Cr^{3+} phosphor with $x = 0.08$ was performed with a microsecond pulse flash-lamp (μF^2) as the excitation light source. The setting parameters are listed as follows: excitation wavelength of 430 nm, test wavelength range of 700–800 nm, delay time of 0–2000 μs, and channel of 2000.

Figure 8(a) presents the time-resolved emission contour map of the optimal NALF:Cr^{3+} phosphor with $x = 0.08$. With increasing delay time from 0 to 600 μs, the emission intensity gradually decreases, while the emission maximum remains nearly unchanged at approximately 721 nm. Unlike Cr^{3+}-activated hosts containing multiple crystallographic sites, no obvious spectral shift toward either shorter or longer wavelengths is observed during the entire decay process. This result indicates that the broadband emission is predominantly associated with Cr^{3+} ions occupying the Al^{3+} octahedral sites. To further verify this conclusion, the emission spectra extracted at different delay times are compared in Figure 8(b). Although the emission intensity decreases continuously with increasing delay time, the spectral profile remains nearly identical throughout the decay process. The absence of significant peak shift or spectral deformation suggests that all delayed emissions arise from the same electronic transition ($^4T_{2g} \rightarrow {}^4A_{2g}$) of Cr^{3+} ions occupying an identical crystallographic environment. Therefore, the biexponential decay behavior observed in the fluorescence-lifetime measurements is unlikely to originate from multiple Cr^{3+} emission centers [39]. Instead, it is more reasonably attributed to different relaxation pathways of the same luminescent center, such as defect-assisted non-radiative relaxation,

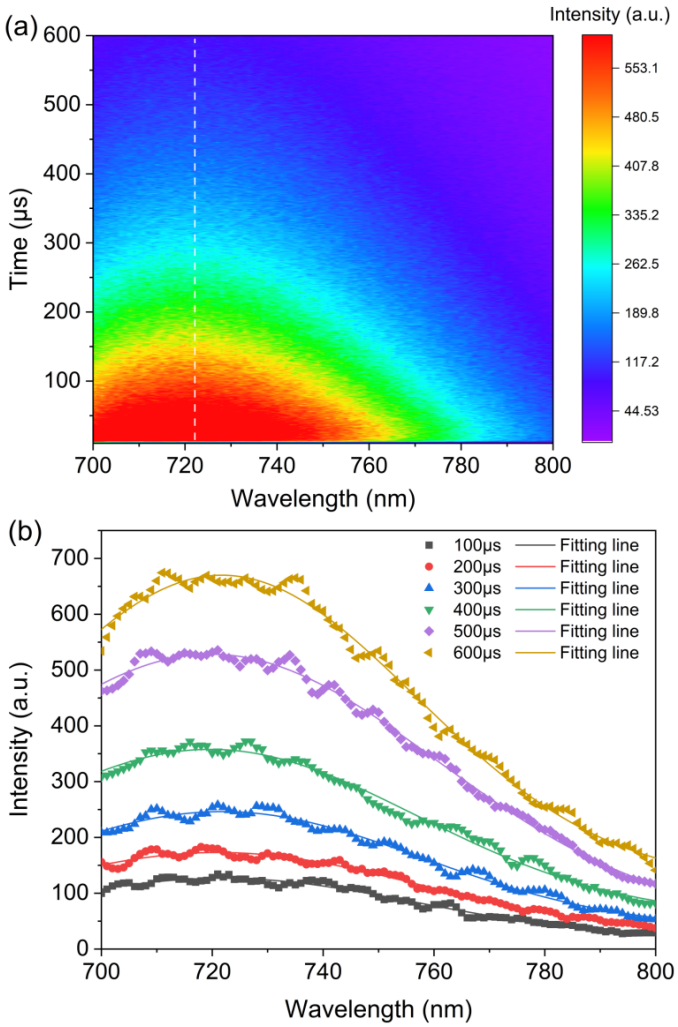

Figure 8. (a) Time-resolved emission spectra and (b) emission spectra under different delay times of the NALF:Cr^{3+} phosphor with $x = 0.08$.

energy migration among neighboring Cr^{3+} ions, or local lattice relaxation around Cr^{3+} ions. The combined lifetime and time-resolved emission results consistently demonstrate that Cr^{3+} ions occupy a single dominant octahedral site in the NALF host and exhibit uniform broadband near-infrared emission characteristics. The longer lifetime component (τ_2) is assigned to isolated Cr^{3+} ions occupying regular Al^{3+} octahedral sites, while the shorter lifetime component (τ_1) is related to defect-associated Cr^{3+} centers or energy migration pathways.

To investigate the thermal stability of the phosphor and elucidate the luminescence behavior of Cr^{3+} ions in the $Na_3Al_2Li_3F_{12}$ host, the sample $x = 0.08$ was selected as a representative and its temperature-dependent PL spectra were recorded over a temperature range of 300–473 K. Figure 9 shows the temperature-dependent PL emission spectra of the NALF:Cr^{3+} phosphor with $x = 0.08$. With increasing temperature, the emission peak gradually red-shifts from approximately 724 nm at RT to 733 nm at 473 K. This red shift can be attributed to thermally induced lattice expansion, which increases the Cr^{3+}–F^- bond lengths and consequently weakens the crystal-field strength (Dq). According to the Tanabe–Sugano diagram, the reduction in crystal-field strength leads to a lowering of the $^4T_{2g}$ excited-state energy level, thereby resulting in the observed red shift of the emission band. Furthermore, at 423 K, the PL intensity of the phosphor still retains more than 67% of its room-temperature value, indicating good thermal stability of the NALF:Cr^{3+} phosphor with $x = 0.08$ and its potential suitability for long-term device applications (Figure 9(c)). To further understand the thermal quenching of the phosphor and the associated electron–phonon coupling process, the activation energy for the thermal-quenching process was calculated using the Arrhenius equation, Eq. (7):

$$I = \frac{I_0}{1 + A\exp\left(-\frac{\Delta E}{kT}\right)} \tag{7}$$

where I and I_0 are the emission intensities at temperature T and RT, respectively; A is a constant; and k is the Boltzmann constant (8.617×10^{-5} eV·K^{-1}). The activation energy ΔE of the NALF:Cr^{3+} phosphor with $x = 0.08$ was determined from the linear relationship between $\ln(I_0/I - 1)$ and $1/(kT)$ (Figure 9(d)). The calculated ΔE for the $x = 0.08$ phosphor is 0.2734(12) eV, indicating that the phosphor possesses good thermal stability of luminescence [32].

To gain insight into the energy-level structure of Cr^{3+} ions in the NALF host, PL spectra were recorded at both 80 K (Figure 10(a)) and RT (Figure 10(b)). Low-temperature measurements effectively suppress thermally activated emission processes and significantly reduce thermal broadening, thereby facilitating a more accurate assignment of the emission transitions. After fitting via Gaussian deconvolution, the RT PL spectrum of the NALF:Cr^{3+} phosphor was deconvoluted into two broad emission bands centered at approximately 1.59 and 1.72 eV. The two Gaussian peaks do not represent two independent luminescent centers. Rather, they are the result of the mathematical deconvolution of the asymmetric $^4T_{2g} \rightarrow {}^4A_{2g}$ emission band associated with a single Cr^{3+} center. This asymmetry arises primarily from two intrinsic physical mechanisms: first, the local

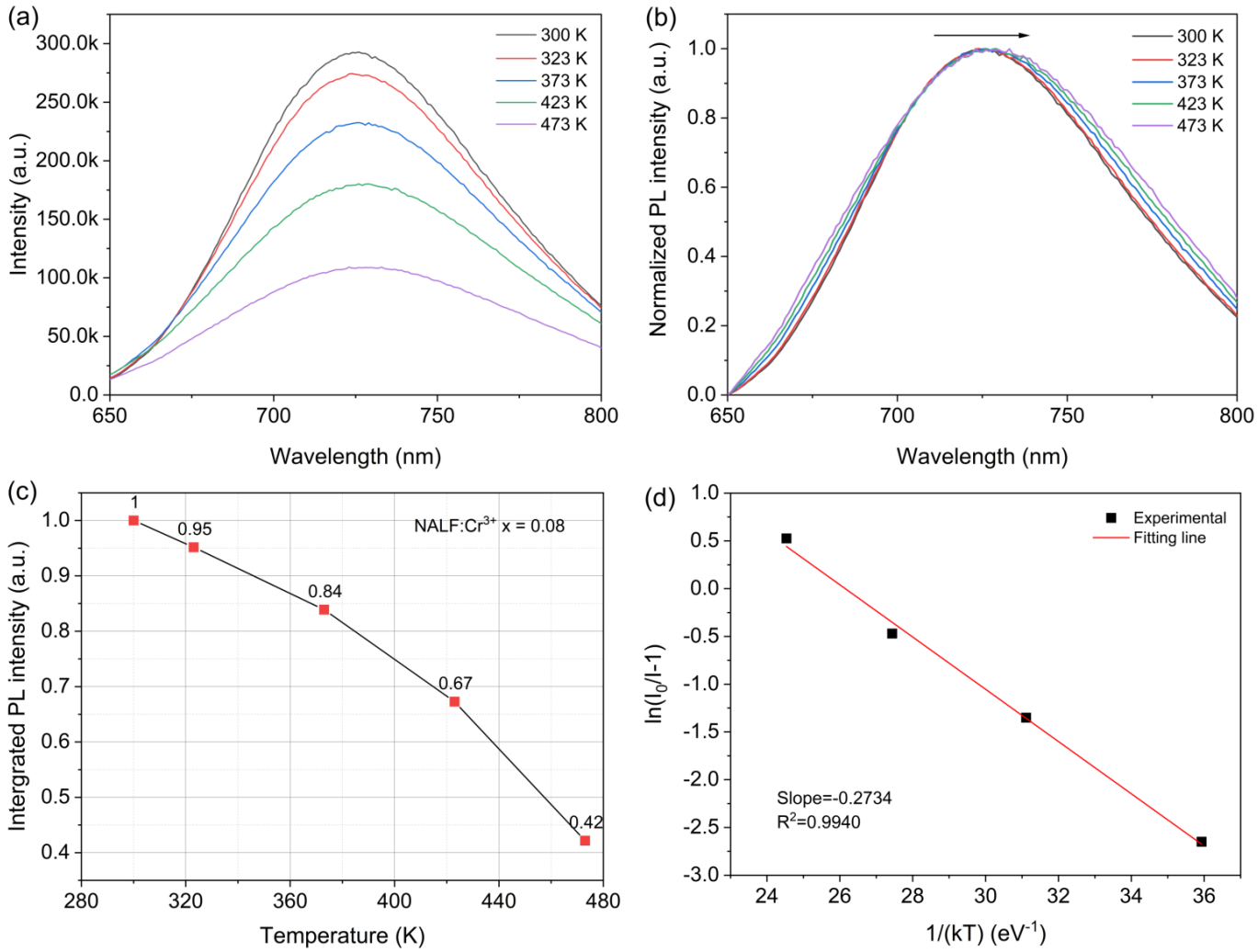

Figure 9. (a) Emission spectra, (b) normalized emission spectra, (c) integrated emission intensities, and (d) linear relationship between $\ln(I_0/I-1)$ and $1/(kT)$ of the NALF:Cr^{3+} phosphor with $x = 0.08$ measured in the temperature range of 300–473 K.

symmetry of the Al^{3+} octahedral site in the host lattice deviates from ideal O_h symmetry, causing Stark splitting of the $^4T_{2g}$ excited state and giving rise to two closely spaced transition channels. Second, strong electron–phonon coupling in the weak crystal field results in an intrinsic tail on the low-energy side of the emission band. Both bands are attributed to the spin-allowed $^4T_{2g} \rightarrow {}^4A_{2g}$ transition of Cr^{3+} ions, indicating that the broadband NIR emission originates from different vibronic components of the same electronic transition. In contrast, the 80 K PL spectrum exhibits a distinctly different spectral profile. Peak fitting reveals three well-resolved emission bands centered at approximately 1.68, 1.74, and 1.80 eV. By comparison with previous reports, the emission peak at 1.80 eV can be assigned to the zero-phonon line (ZPL) of the $^4T_{2g} \rightarrow {}^4A_{2g}$ transition [32, 40, 41]. The emergence of this weak shoulder peak is attributed to the substantial suppression of lattice vibrations at cryogenic temperatures, which weakens electron–phonon coupling and significantly reduces thermal broadening. Consequently, the ZPL becomes distinguishable from the accompanying vibronic emission. In contrast, at RT, strong electron–phonon coupling and thermal broadening broaden the $^4T_{2g} \rightarrow {}^4A_{2g}$ emission band, causing the weak ZPL on the high-energy side to be obscured by the dominant broadband emission. Altogether, the low-temperature spectrum reflects the intrinsic multi-component nature of the broadband emission rather than the formation of a new luminescent center.

4 Conclusion

In summary, pure-phase garnet-type fluoride NALF: Cr^{3+} phosphors were successfully synthesized via a hydrothermal method. The influences of Cr^{3+} concentration on the crystal structure, morphology, and luminescence properties were systematically

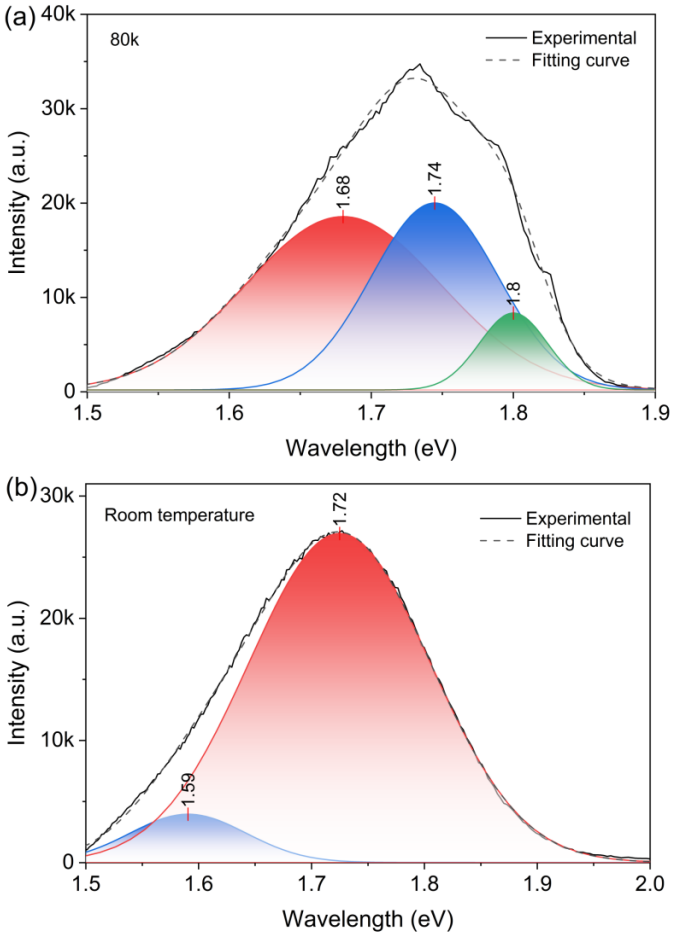

Figure 10. Emission spectra of the NALF:Cr^{3+} phosphor with $x = 0.08$ measured at (a) 80 K and (b) RT.

investigated.

XRD and Rietveld refinement confirmed the formation of a stable single-phase garnet structure over the entire doping range, while FESEM observations revealed that increasing the Cr^{3+} concentration effectively suppressed grain growth. The NALF: Cr^{3+} phosphor exhibits a broad NIR emission band covering 650–900 nm with a FWHM of approximately 101 nm and can be efficiently excited by commercial blue LED chips owing to its strong excitation band centered at 430 nm. Crystal-field analysis based on the absorption spectra and the Tanabe–Sugano diagram yielded a Dq/B value of 2.18, indicating that Cr^{3+} ions reside in a weak crystal-field environment, where broadband NIR emission is dominated by the spin-allowed $^4T_{2g} \rightarrow {}^4A_{2g}$ transition. The fluorescence spectra indicated that the optimal doping concentration of Cr^{3+} is $x = 0.08$, and the sample with this composition exhibits the highest luminescence intensity. The fluorescence decay results showed the presence of two luminescence behaviors of Cr^{3+} in the NALF matrix. Time-resolved emission spectroscopy analysis revealed that the main emission peak position of the sample remains consistent at approximately 721 nm for different delay times, demonstrating that Cr^{3+} only substitutes for Al^{3+} in the octahedral sites in the NALF matrix. These two luminescence behaviors can be attributed to regular Al^{3+} sites and defect-related Al^{3+} sites, respectively. Temperature-dependent PL measurements demonstrated excellent thermal stability, with the emission intensity remaining above 67% of its RT value at 423 K. Furthermore, low-temperature PL spectra revealed the ZPL associated with the $^4T_{2g} \rightarrow {}^4A_{2g}$ transition, providing further insight into the electronic transition mechanism of Cr^{3+} ions in the NALF host.

Overall, the combination of efficient blue-light excitation, broadband NIR emission, favorable thermal stability, and a well-understood luminescence mechanism demonstrates that NALF:Cr^{3+} is a promising phosphor for blue LED-pumped broadband NIR pc-LED applications.

Data Availability Statement

Data will be made available on request.

Funding

This work was supported in part by the National Natural Science Foundation of China under Grant 52502135 and Grant 52402142, in part by the Natural Science Foundation of Henan Province of China under Grant 252300420429, in part by the International Cooperation and Exchange Project of the National Natural Science Foundation of China under Grant W2512070, and in part by the Shanghai Partnership Research Program under Grant 25HB2706600.

Conflicts of Interest

Denis Yu. Kosyanov served as an Editorial Board Member, and Jiang Li served as an Associate Editor of the *Journal of Advanced Materials Research* at the time of manuscript submission. To ensure the integrity of the peer-review process, neither Denis Yu. Kosyanov nor Jiang Li was involved in the editorial handling, peer review, or decision-making process for this manuscript, which was handled independently by another editor. The remaining authors declare no conflicts of interest.

AI Use Statement

The authors declare that no generative AI was used in the preparation of this manuscript.

Ethical Approval and Consent to Participate

Not applicable.

References

[1] Li, H. H., Wang, Y. K., & Liao, L. S. (2024). Near-infrared luminescent materials incorporating rare earth/transition metal ions: from materials to applications. *Advanced Materials, 36*(30), 2403076. [CrossRef]

[2] Hu, Y., Qiao, J., Li, D., Gao, C., & Xia, Z. (2026). Recent developments in near-infrared phosphors for broad-band light-emitting diodes light sources. *Journal of Rare Earths, 44*(6), 1625-1645. [CrossRef]

[3] Yang, Z., Zhang, W., Wang, Z., Zheng, Y., Su, Y., Xu, H., ... & Yang, S. (2025). Efficient and thermally stable Cr^{3+}-activated germanate phosphor for thermometry, plant cultivation, and near-infrared light-emitting diode applications. *Journal of Alloys and Compounds, 1022*, 179931. [CrossRef]

[4] Chen, G., Nie, W., Zuo, J., Li, Y., Han, L., & Ye, X. (2022). A new broadband near-infrared emitting $Mg_2Al_4Si_5O_{18}$:Cr^{3+} phosphor for night-vision imaging. *Dalton Transactions, 51*(33), 12576–12584. CrossRef]

[5] Suo, H., Wang, Y., Zhao, X., Zhang, X., Li, L., Guan, K., ... & Wang, F. (2022). Rapid nondestructive detection enabled by an ultra-broadband NIR pc-LED. *Laser & Photonics Reviews, 16*(7), 2200012. [CrossRef]

[6] Bai, B., Dang, P. P., Zhu, Z. L., Lian, H. Z., & Lin, J. (2020). Broadband near-infrared emission of $La_3Ga_5GeO_{14}$:Tb^{3+},Cr^{3+} phosphors: energy transfer, persistent luminescence and application in NIR light-emitting diodes. *Journal of Materials Chemistry C, 8*(34), 11760-11770. [CrossRef]

[7] Xie, X. D., Wang, C. L., Huang, X. X., Wen, J., Wang, Q., Zhu, M. Y., & Ning, L. X. (2026). Broadband near-infrared emission realized in Fe^{3+}-doped β-Al_2O_3-type structure phosphor via multi-site occupancy for NIR pc-LED applications. *Materials Today Chemistry, 53*, 103586. [CrossRef]

[8] Liu, Y. H., Dou, C., Dou, F., Zhang, Z. H., Gao, X., Zhang, H. Z., Wang, S. T., Wang, X. M., & Jiao, H. (2024). Enhanced NIR emission and thermal stability of La_2MgSnO_6:Mn^{4+},Ni^{2+} via energy transfer. *Journal of Materials Chemistry C, 12*(34), 13508-13515. [CrossRef]

[9] Tang, Z. B., Zhang, Q., Cao, Y. X., Li, Y. X., & Wang, Y. H. (2020). Eu^{2+}-doped ultra-broadband VIS-NIR emitting phosphor. *Chemical Engineering Journal, 388*, 124231. [CrossRef]

[10] Gao, T., Liu, Y., Liu, R., & Zhuang, W. (2023). Research progress and development of near-infrared phosphors. *Materials, 16*(8), 3145. [CrossRef]

[11] Xiang, J., Zheng, J., Zhao, X., Zhou, X., Chen, C., Jin, M., & Guo, C. (2022). Synthesis of broadband NIR garnet phosphor Ca4ZrGe3O12: Cr^{3+}, Yb^{3+} for NIR pc-LED applications. *Materials Chemistry Frontiers, 6*(4), 440-449. [CrossRef]

[12] He, S., Zhang, L., Zhang, J., Hao, Z., Wu, H., Wu, H., ... & Zhang, J. (2022). Cr^{3+} and Nd^{3+} co-activated garnet phosphor for NIR super broadband pc-LED application. *Materials Research Bulletin, 151*, 111797. [CrossRef]

[13] Ma, Y. S., Zhang, X., Yang, X., Ren, Z. H., Zhang, W. Z., Li, X., Guo, Y. N., & Wang, F. H. (2026). Luminescence modulation of blue-LED-excitable Er^{3+}-doped phosphor for both NIR-I and NIR-II emission. *Journal of Luminescence, 293*, 121762. [CrossRef]

[14] Zhang, S., Long, Y., Zhang, P., Fang, Z., Li, Z., Ye, H., ... & Li, Y. (2025). Ultra-transparent β-Ga_2O_3:Cr^{3+} glass-ceramics enabling high-efficiency true-transmission near-infrared light-emitting diodes. *Journal of Advanced Ceramics, 14*(5), 9221075. [CrossRef]

[15] Yue, X. Y., Guo, Y., Xu, J., Hou, Y., Zhu, H. K., Wang, L. X., & Zhang, Q. T. (2024). Thermally stable fluoride phosphor $Na_3Sc_2Li_3F_{12}$:Cr^{3+} with broadband emission for NIR pc-LED applications. *Optical Materials, 149*, 115040. [CrossRef]

[16] Lee, C., Bao, Z., Fang, M. H., Lesniewski, T., Mahlik, S., Grinberg, M., ... & Liu, R. S. (2020). Chromium(III)-doped fluoride phosphors with broadband infrared emission for light-emitting diodes. *Inorganic Chemistry, 59*(1), 376-385. [CrossRef]

[17] Xie, H., Fu, H., Du, Z., Tong, L., Jiang, J., Jiang, X., ... & Zheng, J. (2025). Cr^{3+}-induced broadband near-infrared I combined with near-infrared II emission via rare-earth co-doping in $Cs_2NaInCl_6$ for multifunctional detection. *Journal of Materials Chemistry C, 13*(28), 14648-14656. [CrossRef]

[18] Liao, Y., Yao, L., Liu, S., Zhang, Z., He, L., Wang, J., ... & Ye, X. (2025). Near-infrared luminescence regulation and imaging applications of novel Cr^{3+}-doped double-perovskite-structured tantalate phosphors. *Journal of Alloys and Compounds, 1010*, 177991. [CrossRef]

[19] Yang, J., Yuan, L. F., Qian, D., Wu, H. Y., & Jin, Y. H. (2024). Highly thermal-stable broadband near-infrared emission of Cr^{3+}-doped spinel $CdGa_2O_4$ phosphors. *Journal of Luminescence, 275*, 120825. [CrossRef]

[20] Liu, S. Q., Du, J. X., Song, Z., Ma, C. G., & Liu, Q. L. (2023). Intervalence charge transfer of Cr^{3+}-Cr^{3+} aggregation for NIR-II luminescence. *Light: Science & Applications, 12*(1), 181. [CrossRef]

[21] Jia, Z., Yuan, C., Liu, Y., Wang, X. J., Sun, P., Wang, L., ... & Jiang, J. (2020). Strategies to approach high performance in Cr3+-doped phosphors for high-power NIR-LED light sources. *Light: Science & Applications, 9*(1), 86. [CrossRef]

[22] Jiang, H. J., Chen, L. Y., Zheng, G. J., Luo,

Z. H., Wu, X. H., Liu, Z. H., Liu, R. Y., Liu, Y. F., Sun, P., & Jiang, J. (2022). Ultra-efficient GAGG:Cr^{3+} ceramic phosphor-converted laser diode: a promising high-power compact near-infrared light source enabling clear imaging. *Advanced Optical Materials, 10*(11), 2102741. [CrossRef]

[23] Li, C., & Zhong, J. (2022). Highly efficient broadband near-infrared luminescence with zero-thermal-quenching in garnet Y3In2Ga3O12: Cr3+ phosphors. *Chemistry of Materials, 34*(18), 8418-8426. [CrossRef]

[24] Basore, E. T., Xiao, W. G., Liu, X. F., Wu, J. H., & Qiu, J. R. (2020). Broadband near-infrared garnet phosphors with near-unity internal quantum efficiency. *Advanced Optical Materials, 8*(12), 2000296. [CrossRef]

[25] Ma, Y., Li, X., Wu, L., Shao, C. Y., Zhang, B. Q., Pang, T., ... & Chen, D. Q. (2024). Preparation of $(Lu,Y)_3(Al,Sc,Cr)_2Al_3O_{12}$ phosphor ceramics with high thermal stability for near-infrared LED/LD. *Journal of Advanced Ceramics, 13*(3), 354-363. [CrossRef]

[26] Lin, Q., Wang, Q., Liao, M., Xiong, M., Feng, X., Zhang, X., ... & Mu, Z. (2021). Trivalent chromium ions doped fluorides with both broad emission bandwidth and excellent luminescence thermal stability. *ACS applied materials & interfaces, 13*(15), 18274-18282. [CrossRef]

[27] Li, Y., Yu, X., An, X. M., Tan, Q. L., Liu, H. J., Li, Z. Z., & Zhang, S. A. (2024). $Li_3Na_3Ga_2F_{12}$:Cr^{3+} fluoride wideband near-infrared fluorescence material synthesized by a green method. *Laser & Optoelectronics Progress*, 61, 0316004. [CrossRef]

[28] Dang, P., Wei, Y., Liu, D., Li, G., & Lin, J. (2023). Recent advances in chromium-doped near-infrared luminescent materials: fundamentals, optimization strategies, and applications. *Advanced Optical Materials, 11*(3), 2201739. [CrossRef]

[29] Zhu, M. M., Pan, Y. X., Xi, L. Q., Lian, H. Z., & Lin, J. (2017). Design, preparation, and optimized luminescence of a dodec-fluoride phosphor $Li_3Na_3Al_2F_{12}$:Mn^{4+} for warm WLEDs application. *Journal of Materials Chemistry C, 5*(39), 10241-10250. [CrossRef]

[30] Song, E., Ming, H., Zhou, Y., He, F., Wu, J., Xia, Z., & Zhang, Q. (2021). Cr3+-Doped Sc-based fluoride enabling highly efficient near infrared luminescence: a case study of K2NaScF6: Cr3+. *Laser & Photonics Reviews, 15*(2), 2000410. [CrossRef]

[31] Fan, Q., Wan, J., Wang, Z., Zhong, L., Jiang, C., Zhou, Q., ... & Wu, M. (2026). Recent advances in Cr^{3+}-doped near-infrared phosphors: preparation, luminescence, and LED applications. Inorganic Chemistry Frontiers, 13(8), 3237-3263.. [CrossRef]

[32] Huang, D. C., Liang, S. S., Chen, D. J., Hu, J., Xu, K. Y., & Zhu, H. M. (2021). An efficient garnet-structured $Na_3Al_2Li_3F_{12}$:Cr^{3+} phosphor with excellent photoluminescence thermal stability for near-infrared LEDs. *Chemical Engineering Journal, 426*, 131332. [CrossRef]

[33] Nie, W. D., Li, Y., Zuo, J. X., Kong, Y. K., Zou, W. F., Chen, G., Peng, J. Q., Du, F., Han, L., & Ye, X. Y. (2021). Cr^{3+}-activated $Na_3X_2Li_3F_{12}$ (X = Al, Ga, or In) garnet phosphors with broadband NIR emission and high luminescence efficiency for potential biomedical application. *Journal of Materials Chemistry C, 9*(42), 15230-15241. [CrossRef]

[34] Takeda, Y., Sone, M., Suwa, Y., Inagaki, M., & Naka, S. (1977). Synthesis of fluoride garnets $Na_3[M_2^{3+}](Li_3)F_{12}$ (M = Al, Cr, and Fe) from aqueous solution and their properties. *Journal of Solid State Chemistry, 20*(3), 261-265. [CrossRef]

[35] Shannon, R. D. (1976). Revised effective ionic radii and systematic studies of interatomic distances in halides and chalcogenides. *Acta Crystallographica Section A, 32*(5), 751-767. [CrossRef]

[36] Zhang, C. H., Yi, G. Q., Sun, Z. C., & Mei, B. C. (2023). Cr^{3+}-doped CaF_2 transparent ceramic with effective broadband near-infrared emission. *Materials Letters, 346*, 134506. [CrossRef]

[37] Lempicki, A., Andrews, L., Nettel, S. J., McCollum, B. C., & Solomon, I. (1980). Spectroscopy of Cr^{3+} in glasses: Fano antiresonances and vibronic "Lamb shift". *Physical Review Letters, 44*(18), 1234-1237. [CrossRef]

[38] Li, T. S., Wang, W. L., Liu, Q., Wang, Y. B., Zhou, Z. Z., Hu, C., & Li, J. (2025). Influence of Cr^{3+} doping concentration on the persistent performance of YAGG:Ce^{3+},Cr^{3+} luminescent ceramics. *Journal of Inorganic Materials, 40*(9), 1037-1044. [CrossRef]

[39] Cheng, M., Chen, Z. Q., Zhou, Y. Y., Ren, P., Zhou, Q., Tang, H. J., & Wang, Z. L. (2025). A broadband near-infrared phosphor: solid-state synthesis, two Cr^{3+} sites occupation and enhanced thermal stability. *Journal of Luminescence, 277*, 120971. [CrossRef]

[40] Caird, J. A., Payne, S. A., Staver, P. R., Ramponi, A. J., Chase, L. L., & Krupke, W. E. (1988). Quantum electronic properties of the $Na_3Ga_2Li_3F_{12}$:Cr^{3+} laser. *IEEE Journal of Quantum Electronics, 24*(6), 1077-1099. [CrossRef]

[41] Adachi, S. (2021). photoluminescence properties of Cr^{3+}-activated fluoride phosphors. *ECS Journal of Solid State Science and Technology, 10*(2), 026001. [CrossRef]

Xinlei Zang is currently a master's student at the Henan University of Technology. He received his Bachelor of Engineering from the School of Materials Science and Engineering, Henan University of Technology in 2023. His postgraduate research focuses on the rare earth ion doped garnet based fluorescent ceramics and transition metal ion doped fluoride phosphors for high-power lighting. (E-mail: 1870765812@qq.com)

Yagang Feng is an associate professor of the Henan University of Technology. His research interests focus on the rare earth ions doped optical-functional transparent ceramics for laser and fluorescence applications, including the garnet-based ceramics and fluoride ceramics. (E-mail: yagangfeng@haut.edu.cn)

Yumeng Li is currently a master student at the Henan University of Technology. She received her Bachelor of Engineering from the School of Materials Science and Engineering, Henan University of Technology in 2024. Her postgraduate research focuses on the performance optimization of rare earth ion doped fluoride fluorescent powder for white LED. (E-mail: kblzs1992@163.com)

Ziyu Liu is a lecturer and master supervisor of the Changsha University of Science & Technology. Her research direction is advanced ceramic technology that integrates structure and function. Her research topics include transparent light functional ceramics, oxide ceramic powders, and special ceramic materials that integrate structure and function.(ziyuliu@csust.edu.cn)

Lei Duan is an associate professor at the School of Materials Science & Engineering, Henan University of Technology. His research interests focus on using high pressure technique to explore and synthesize new quantum materials such as superconductors and quasi one-dimensional (1D) materials. (E-mail: lei_duan@haut.edu.cn)

Shichang Cai is a lecturer at the School of Materials Science & Engineering, Henan University of Technology. His research interests focus on the porous carbon-based catalytic materials for energy conversion, including fuel cells and zinc-air batteries. (E-mail: caishichang@whut.edu.cn)

Hanlu Zhang is a lecturer at the School of Materials Science & Engineering, Henan University of Technology. His research interests focus on the two dimensional semiconductor optoelectronic materials, electret electromechanical conversion devices, fluorescent powders, conductive metal micro powders. (E-mail: hanlu_zhang@haut.edu.cn)

Chen Hu is an associate professor of Shanghai Institute of Ceramics, Chinese Academy of Sciences. His research interests mainly focuses on scintillation ceramics. (E-mail: huchen@mail.sic.ac.cn)

Zhenzhen Zhou is an associate professor of the Shanghai Institute of Ceramics, Chinese Academy of Sciences. Her current research primarily focuses on optical functional ceramics, including ceramic phosphors and ceramic scintillators. (E-mail: zhouzhenzhen@mail.sic.ac.cn)

Denis Yu. Kosyanov Ph.D., is a Researcher at the Far Eastern Federal University, 10 Ajax Bay, Russky Island. His research interests include fabrication of oxide nanopowders; solid-state and spark plasma sintering of nanopowders; structural-phase state and microstructural analysis of optical ceramics. (E-mail: kosianov.diu@dvfu.ru)

Jiang Li is a professor of Shanghai Institute of Ceramics, Chinese Academy of Sciences (SICCAS). Now he is the deputy director of the transparent ceramics research centre in SICCAS, the associate editors of the Journal of Advanced Ceramics, Journal of Inorganic Materials, and Journal of the American Ceramic Society. Prof. Li's research focuses on laser ceramics, scintillation ceramics, magneto-optical ceramics, ceramic phosphors, and other optical transparent ceramics. He has been selected for four consecutive years as the global top 2% scientists "Lifetime Scientific Impact Rankings" list (2024 edition) released by Stanford University. He was invited to give invited reports in the academic conferences for more than 100 times. He is the coordinator in more than 25 domestic and 8 international collaborative projects so far in the field of transparent and opto-functional ceramics. He produced 501 original papers (10366 Citations, 48 H-index) in refereed journals, 3 co-authored textbooks and 2 co-authored book chapters. (E-mail: lijiang@mail.sic.ac.cn)